Corrosion Science 228 (2024) 111820

Contents lists available at ScienceDirect

Corrosion Science

journal homepage: www.elsevier.com/locate/corsci

Highly dense passivation enhanced corrosion resistance of Ti_2AlC MAX phase coating in 3.5 wt.% NaCl solution

Zhongchang Li [a,b,1], Yan Zhang [a,1], Kaihang Wang [a,b], Zhenyu Wang [a,*], Guanshui Ma [a], Peiling Ke [a,b], Aiying Wang [a,b,**]

[a] Key Laboratory of Marine Materials and Related Technologies, Zhejiang Key Laboratory of Marine Materials and Protective Technologies, Ningbo Institute of Materials Technology and Engineering, Chinese Academy of Sciences, Ningbo 315201, China
[b] Center of Materials Science and Optoelectronics Engineering, University of Chinese Academy of Sciences, Beijing 100049, China

ARTICLE INFO

Keywords:
Ti_2AlC coating
Passive films
Densely amorphous Al_2O_3
Corrosion resistance
DFT

ABSTRACT

This study aimed to investigate the dependence of electrochemical behavior upon the microstructural evolution of Ti_2AlC MAX phase coating in 3.5 wt.% NaCl solution. The results showed that high-purity Ti_2AlC coating with unique equiaxed nanocrystals exhibited remarkably higher impedance and lower current densities compared to those of uncoated Ti-6Al-4V substrate, which was attributed to the formed highly dense and continuously amorphous Al_2O_3 passive film on the coating surface. According to the combined DFT calculations, both the large diffusivity of Al atoms and the robust stability of Ti_2Al_xC with Al vacancies exceeding 50% contributed to the unusual achievement of electrochemical passivation characteristics, enabling the significant enhancement of anti-corrosion capability for Ti_2AlC coating.

1. Introduction

With the rapid development of high thrust-to-weight ratio aerocrafts, titanium alloys have drawn increasing attention as one of the most popular metallic materials substituting Ni-based superalloys due to their combinational properties of low density, high strength-to-weight ratio, good corrosion resistance, and easy formability as well [1–3]. However, once the engines work in the harsh marine environment with strong chloride and highly humid media, the recycled actions of parking or landing will easily lead to severe eutectic salt deposition on the component surfaces, accelerating the performance deterioration of engine blades. These damages are particularly critical for Ti-based blades, in which erosion failure and repetitive electrochemical invalidation have been stimulated rapidly under salt-coupled hot oxidations [4–6]. As the aforementioned erosion and corrosion are strongly related to surface-dominated damages, extensive efforts have been dedicated to improving the wear and corrosion behavior of titanium alloys via various surface modifications, such as plasma spraying [7], chemical vapor deposition (CVD) [8], physical vapor deposition (PVD) [9], nitriding [10] and ion implantation [11,12]. Among these techniques, ceramic nitride and carbide hard coatings with nanocrystalline structures offer a unique advantage in providing comprehensive protection for titanium alloys while retaining the superior features of the substrate simultaneously [13,14]. For example, a series of nanocrystalline hard coatings like TiN, NbN and TiCN have demonstrated the favorable enhancement of tribological and electrochemical properties for Ti-6Al-4V alloys [15,16]. For the cases of harsh corrosion, nevertheless, both the intrinsic brittleness and the deposited columnar structure render the ceramic hard coatings apt to be worn due to the facile penetration and rapid diffusion pathway for corrosive media like chloride and oxygen. Therefore, it is of great necessity to achieve dense coatings with hard yet tough properties and alternatively, to explore other protective coatings against the harsh marine environment.

As defined by Barsoum, $M_{n+1}AX_n$ phases (MAX phases, n = 1–3) emerge as a new type of ternary nano-laminated nitrides and carbides, where M belongs to an early transition metal, A refers to A-group elements mainly from IIIA or IVA, and C is either carbon or nitrogen [17,18]. Thanks to the unique presence of weak M-A metallic and strong

* Corresponding author.
** Corresponding author at: Key Laboratory of Marine Materials and Related Technologies, Zhejiang Key Laboratory of Marine Materials and Protective Technologies, Ningbo Institute of Materials Technology and Engineering, Chinese Academy of Sciences, Ningbo 315201, China.
E-mail addresses: wangzy@nimte.ac.cn (Z. Wang), aywang@nimte.ac.cn (A. Wang).
[1] These authors contributed equally to this work

https://doi.org/10.1016/j.corsci.2024.111820
Received 29 July 2023; Received in revised form 28 December 2023; Accepted 2 January 2024
Available online 5 January 2024
0010-938X/© 2024 Elsevier Ltd. All rights reserved.

covalent bonds in the crystals, together with the special nano-laminar hexagonal-structure, MAX phases demonstrate remarkably combinational properties of metals and ceramics, which include excellent machinability, good electrical conductivity, high strength and elastic modulus, superior oxidation resistance, as well as strong anti-corrosion capability. Recently, MAX phase materials have specially drawn increased scientific and technical interest as protective wear-resistance and corrosion-resistance coatings for mechanical components operating in harsh environments [19,20]. In particular, Ti_2AlC MAX phase coating is the most promising for sea-related Ti-based alloy blades because of its low density of 4.1 g/cm^3, excellent thermal shock resistance, and remarkable chemical stability over a wide range of temperatures [21,22]. When the Ti_2AlC coating was conducted under NaCl media with water vapor at 600 °C, the observation of densely amorphous Al_2O_3 phases was reported, which substantially enhanced the corrosion resistance of the coating to the salt-couple hot condition, showing a strong self-healing capability [23]. In addition, excellent self-lubrication with friction coefficients around 0.29–0.38 was achieved for Ti_2AlC coating in a temperature range of 25–800 °C [24], which reduced substrate stress by 41.3% and suppressed cracking. If one considers the importance of facile synthesis for the coating, another competitive advantage for Ti_2AlC coating is the relatively low temperature and the broad phase-forming region compared to other MAX phase candidates [25]. However, it noted that there is still a lack of studies on the corrosion behavior of Ti_2AlC coating in aqueous or even corrosive media for marine applications.

Meanwhile, traditional PVD techniques like magnetron sputtering and cathodic vacuum arc, which are currently dominating methods for synthesizing MAX phase coatings, easily make the coatings with composition impurities and growth defects like macroparticles, pinholes, and coarse crystals, as well as poor adhesion strength during the synthesis process [26]. High power impulse magnetron sputtering (HiPIMS), utilizing extremely high current densities in short pulse at a lower duty cycle (on-off time ratio <10%), shows the advantages of high ionization rate, low-temperature deposition, and high controllability than traditional sputtering [27]. Furthermore, the higher incident energy in HiPIMS significantly promotes the diffusion and surface migration of sputtered species, as well as distinctly reduces the presence of large droplets on the coating surface. All these merits contribute to highly dense, smooth surface, and strong adhesion of the deposited coatings on the substrate. Most importantly, the performance of coating can be widely controlled by varying the discharged dense plasma with different ionization rates, which provides a promising strategy to improve the anti-corrosion properties of MAX phase coatings.

In our previous work, the Ti_3AlC_2 MAX phase coating with high purity and good mechanical properties was successfully synthesized by a hybrid HiPIMS technique and followed annealing at a low temperature of 700 °C [28], while the Ti_2AlC coating was only obtained by the same DCMS annealing processes. The reason was identified by the higher ionization and plasma incident energy in HiPIMS than in DCMS. However, the Ti_3AlC_2 coating displayed a lower hardness than Ti_2AlC, indicating the poor capability to endure wear erosion. Therefore, in this work, taking advantage of controlled ionization rate and incident ion energy, we specifically synthesized the Ti_2AlC MAX phase coating on Ti-6Al-4V substrate using a two-step method with HiPIMS technique and vacuum annealing. The corrosion behavior of the coating in 3.5 wt.% NaCl solution was investigated by comprehensive experiments and calculations. Both the potentiodynamic polarization curve and ac impedance spectroscopy were used to address the electrochemical properties of Ti_2AlC coating. The passivation characteristics under applied anodic potentials were discussed in terms of the microstructural evolution and the atomic calculations by the DFT method.

2. Experimental procedure

2.1. Coating preparation

The Ti_2AlC MAX phase coating was synthesized on the Ti-6Al-4V substrate by a hybrid two-step approach involving the HiPIMS deposition and subsequent thermal annealing. The substrate size of Ti-6Al-4V alloy was 30 mm × 10 mm in square and 3 mm in thickness, with the nominal composition of Al, 6.04; V, 4.03; Fe, 0.3; O, 0.1; C, 0.1; N, 0.05; H, 0.015; and the balance, Ti. The substrate was ground using a sequence of 400–2000 grit silicon carbide papers and then polished with 1.5 μm diamond paste to a mirrored-like appearance. The polished substrate was subsequently subjected to ultrasonic cleaning in acetone and alcohol for 10 min each, followed by air drying before being loaded into the substrate holder within a vacuum chamber.

In the first step, a home-made magnetron sputtering system with multi-target sources (SKY Technology Development Co. Ltd., Shenyang, China) was used to deposit the as-deposited Ti-Al-C coating. Specifically, the HiPIMS power supply was introduced to the compound TiAl target (1:1 at. ratio). In contrast, the DC power supply was applied to the graphite carbon target to balance the sputtering yield between Ti, Al and C elements [29]. Fig. 1a shows the schematic diagram of the co-sputtering HiPIMS system, while Fig. 1b displays an in-situ photography of plasma discharge during coating deposition. When the base pressure of the chamber was evacuated down to 2×10^{-3} Pa, the substrate was heated to 400 °C for degassing. Furthermore, the substrate was etched in Ar^+ plasma at 2 Pa for 30 min with a negative bias of −400 V to remove the adsorbed surface contaminants. Subsequently, the TiAl compound target with HiPIMS mode was conducted to fabricate a TiAl buffer layer at a duty cycle of 5% for 0.5 h, which could suppress the interdiffusion of elements during the next annealing. Then, the co-sputtering of the graphite target by DCMS mode was operated to deposit the Ti-Al-C coating, with a deposition time of 6 h. The substrate temperature was fixed at 300 °C, and a pulsed −100 V was applied to the substrate for all deposition. The working pressure was about 0.7 Pa. In addition, the substrate holder was rotated during deposition to improve the coating uniformity. The detailed parameters for the deposition process are illustrated in Table 1.

In the second step, ex-situ annealing was carried out to transform the as-deposited coating into the crystalline Ti_2AlC MAX phase using a quartz-tube furnace. Namely, the as-deposited Ti-Al-C coating underwent annealing at 700 °C for 1.5 h, during which the pressure was controlled at 2×10^{-3} Pa and the heating rate was fixed at 10 ºC/min. After the annealing, natural cooling was performed for the sample finally. Fig. 1c illustrates the schematic diagram of the annealing process for the as-deposited coating, which shows the successful transformation of the Ti-Al-C coating into the Ti_2AlC MAX phase after treatment.

2.2. Electrochemical measurements

All electrochemical measurements were undertaken using a Reference 600 + electrochemical workstation (Gamry, USA) in a conventional three-electrode configuration, which consisted of a test specimen with an exposed area of ~ 0.2 cm^2 as the working electrode, a platinum wire as a counter electrode and an Ag/AgCl electrode as reference. The working electrolyte of 3.5 wt.% NaCl solution was prepared with analytically pure reagents and distilled water for simulating the marine environment, corresponding to the pH value of around 7. Before the electrochemical experiment, each test specimen underwent an open circuit potential (OCP) measurement with 10 min duration, followed by 5 min of cathodic polarization at −0.8 V vs. the initial E_{OCP}. The purpose was to reduce the air-formed oxide on the sample surface and stabilize the initial surface conditions. Similar treatment has been previously reported [30,31]. Subsequently, a stable open circuit potential value was usually achieved after continuous immersion for 60 min. The potentiodynamic polarization curves were recorded from −0.50 to

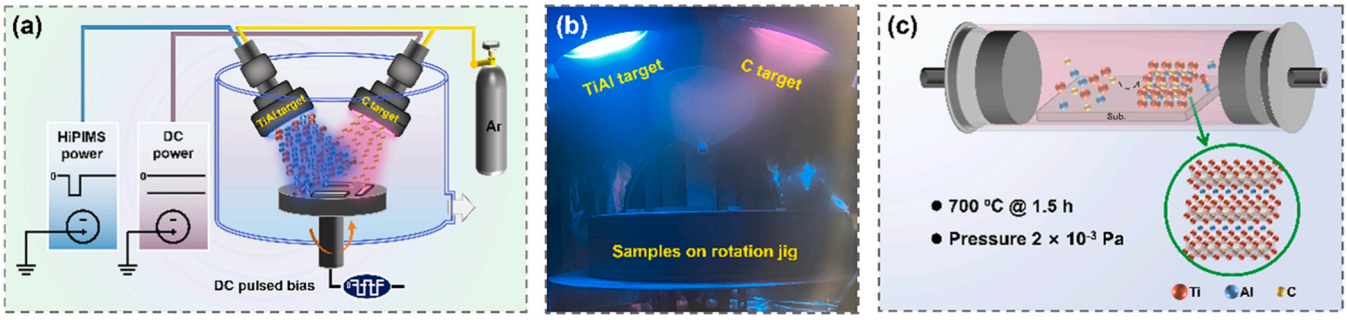

Fig. 1. Schematic of the coating preparation process: (a) multi-target magnetron sputtering system; (b) photograph of discharge plasma for TiAl and C targets; (c) formation of Ti_2AlC coating by subsequent annealing.

Table 1
Deposition parameters for the TiAl interface layer and Ti-Al-C layer.

Deposition process	TiAl target			C target	*p* [Pa]	T [°C]	Ar [sccm]	Bias [V]
	Duty ratio [%]	F [Hz]	P [W]	P [W]				
Ar^+ etching	-	-	-	-	2	400	2	-400
TiAl interface layer	5	1000	123	-	0.7	300	20	-100
Ti-Al-C layer	5	1000	123	75	0.7	300	20	-100

+1.50 V vs. the stable E_{OCP} with a scan rate of 1 mV s^{-1}. The electrochemical impedance spectroscopy (EIS) measurements were conducted under the respective stable E_{OCP} and after potentiostatic polarization at different potentials with a perturbing AC amplitude of 10 mV over a frequency range from 100 kHz to 10 mHz. The obtained EIS data were analyzed using the ZsimpWin software to fit the measured data numerically, which was available for the establishment of equivalent electric circuits (EEC). Moreover, the Mott-Schottky measurements were conducted on the passive films at a fixed frequency of 1 kHz by performing a potential scan towards the negative direction with steps of 100 mV. All tests were repeated in the same conditions at least three times to confirm the experimental reproducibility. The most representative results were used for discussion in the present study.

2.3. Characterization methods

The phase structure of the as-prepared coating was characterized by X-ray diffractogram (XRD, D8-Advance Brucker) using Cu K_α irradiation ($\lambda = 0.15406$ nm), with a step rate of 0.5°/min over diffraction angle range from 5° to 90°. The surface morphologies of the coating were achieved by scanning electron microscopy (SEM, S-4800, Japan). Chemical compositions after corrosion tests were determined through X-ray photoelectron spectroscopy (XPS) measurements on an AXIS SUPRA spectrometer (Kratos), using a monochromatic Al Kα ($h\nu$=1486.6 eV) with an emission current of 10 mA and a voltage of 15 kV. The survey spectra were recorded at a pass energy of 160 eV with an energy step of 1.0 eV, whereas the high-resolution spectra were recorded at a pass energy of 20 eV with an energy step of 0.05 eV. Moreover, the depth profiles were performed to analyze the distribution of chemical compositions in the passive films. An argon gun operating at 5 keV was carried to sputter the sample surface in the profile analyses. All XPS peak positions were calibrated by referencing the C 1 s peak from adventitious carbon with a binding energy of 284.8 eV. The Shirley background, Gaussian and mixed Gaussian/Lorentzian functions were used for the peak fitting procedure. In addition, the chemical compositions of the aqueous solutions after electrochemical tests were collected by Inductively Coupled Plasma-Optical Emission Spectrometer (ICP-OES, SPECTRO ARCOS).

Further detailed observations of the as-prepared coating and the corrosion passive film were accomplished with a TF-20 electron microscope operating at 200 kV, including cross-sectional transmission electron microscopy (TEM), selected-area electron diffractogram (SAED) and high-resolution TEM (HRTEM). Particularly, the grain size of Ti_2AlC coating was estimated using TEM dark-field (DF) and scanning TEM low-angle-annular-dark-field (STEM-ADF) imaging. Furthermore, the Energy dispersive X-ray spectroscopy (EDS) qualitative maps and line scans across the formed passive film to the coating were acquired in the scanning TEM high-angle-annular-dark-field (STEM-HADDF) mode equipped with an EDS detector. All the TEM specimens were prepared using a focused ion beam (FIB, Helios-G4-CX, Thermo Scientific). Besides, a protective carbon layer was deposited before cutting the TEM sample of the passive film to avoid scaling of the oxide layer.

The adhesion strength between coating and substrate was determined by scratch tester (CSM Revetest, Switzerland) under constant load mode, where a diamond Rockwell conical indenter with an approximated apex angle of 120° and a curvature radius of 200 μm was used. During the progressive scratch test, the indenter was loaded continuously from 1 N to 100 N with a scratch speed of 1.00 mm/min. The critical load where the coating was completely peeled off was determined to be the adhesion strength.

2.4. Atomic calculations

The Cambridge Sequential Total Energy Package (CASTEP) code was employed to accomplish atomic investigations of Ti_2AlC structure via density functional theory (DFT) based on the plane–wave pseudopotential method [32]. Especially, the generalized gradient approximation constructed by Perdew-Burke-Ernzerhof (GGA-PBE) [33] was adopted for the exchange-correlation energy function. For all calculations, the plane wave energy cutoff was set at 480 eV and the Brillouin zone sampling was 5 × 5 × 2 k-point meshes. A 2 × 2 × 1 supercell with 32 atoms was constructed to simulate the structural evolution and defect formation related to the convergence test.

The mono-vacancy structure of Ti_2AlC was represented by a 2 × 2 × 1 supercell containing 31 atoms after removing one atom from each species. In addition, the self-diffusion barrier of each species in the Ti_2AlC mode was calculated by searching the transition state linking the two end defective configurations, which was realized by the neighboring vacancy jump along the basal plane. The method employed to locate the transition state structure through reaction coordinates was called LST/QST algorithm, combining the linear (LST) or quadratic synchronous transit (QST) methods with conjugate gradient (CG) refinements [34].

3. Results and discussion

3.1. Characterization of as-prepared Ti_2AlC MAX phase coating

Fig. 2a reveals the X-ray diffractogram for the as-prepared Ti_2AlC coating on the Ti-6Al-4V substrate. Based on the standard powder diffractogram data, most of the diffractogram peaks were identified as the features of the Ti_2AlC MAX phase except those of the substrate. Noted that, although a small number of peaks assigned to the presence of titanium-aluminum intermetallic compounds were also visible in the XRD spectrum, the peak intensity was too weak to be addressed. This observation indicated the predominant high-purity Ti_2AlC MAX phase in the coating, with (103) preferential orientation. In addition, the surface morphology of the Ti_2AlC coating shown in Fig. 2b was relatively smooth, compact, and uniform. The enlarged image inserted in Fig. 2b also confirmed the observation without defects like macro-particles, pinholes and microcracks in the coating. Furthermore, Fig. 2c displays the cross-sectional image and the corresponding EDS analysis of the coating. Three different regions could be clearly identified in the cross-sectional morphology, i.e., Ti_2AlC layer, interface layer and substrate. The line-scanning of EDS along with the element mapping highlighted the enrichment of the Al element at the interface, as marked by the white-dashed rectangle in the line-scanning spectrum. This evidenced that the coating consisted of a ~0.5 μm-thick inner $TiAl_x$ layer and a 2.5 μm-thick outer Ti_2AlC layer, in which the chemical compositions of Ti, Al, and C were distributed uniformly along the growth direction. Table 2 lists the element composition of EDS point scanning as shown in Fig. 2c, which agreed well with the line-scanning and mapping results. Another important observation was that the bond interface between coating and substrate was relatively sharp and clear, without any distinct defects such as cracks and delamination. Consequently, it could be concluded that the achieved Ti_2AlC MAX phase coating was extremely dense and homogenous, together with strong adhesion bonded to the substrate. The reason for this observation could be originated from the remarkable combination of high ionization rate and heavy incident ion energy during HiPIMS technique, which in turn promoted the diffusion and surface mobility of deposited adatoms, similar to previous work [35].

Table 2
Element composition of EDS points as shown in Fig. 2c.

Point	Ti (at%)	Al (at%)	C (at%)
1	46.17	27.63	26.20
2	49.02	46.56	4.42

To elucidate the microstructure of as-prepared Ti_2AlC coating, Fig. 3 shows the TEM results with the phase structure and the grain size distribution. According to the bright-field image in Fig. 3a and dark-field image in Fig. 3b, the Ti_2AlC coating was composed of uniformly distributed equiaxed grains, where the average grain size was calculated to be around 38.83 nm (Fig. 3d). Further characterization of the concentric diffraction rings in SAED (Fig. 3c) showed that the distinct intensity of the (103) plane was found in accordance with the XRD data. The high-resolution TEM (HRTEM) image and the corresponding enlarged view of the area marked by the red frame are depicted in Fig. 3e and f, respectively. A typical nanolaminated structure belonging to the MAX phase could be clearly observed, composed of alternating two Ti(C) layers and one Al layer. The measured adjacent lattice fringe spacing of 0.68 nm was in accordance with the theoretical value corresponding to the (002) crystallographic plane of the Ti_2AlC phase. Moreover, the atom stacking sequence of the Ti_2AlC was identified along the $[11\bar{2}0]$ direction, which was assigned to A$\underline{B}$A$\underline{B}$A$\underline{B}$ (where the underlined letters referred to Al atomic layers and other letters referred to Ti atomic layers). Noted that the C atoms could not be isolated even from STEM because of their weak diffractogram power, the *c* lattice parameter was calculated to be 1.36 nm from the STEM image, in line with the standard value of the Ti_2AlC MAX phase.

Fig. 4 shows the adhesion strength of the as-prepared Ti_2AlC coating

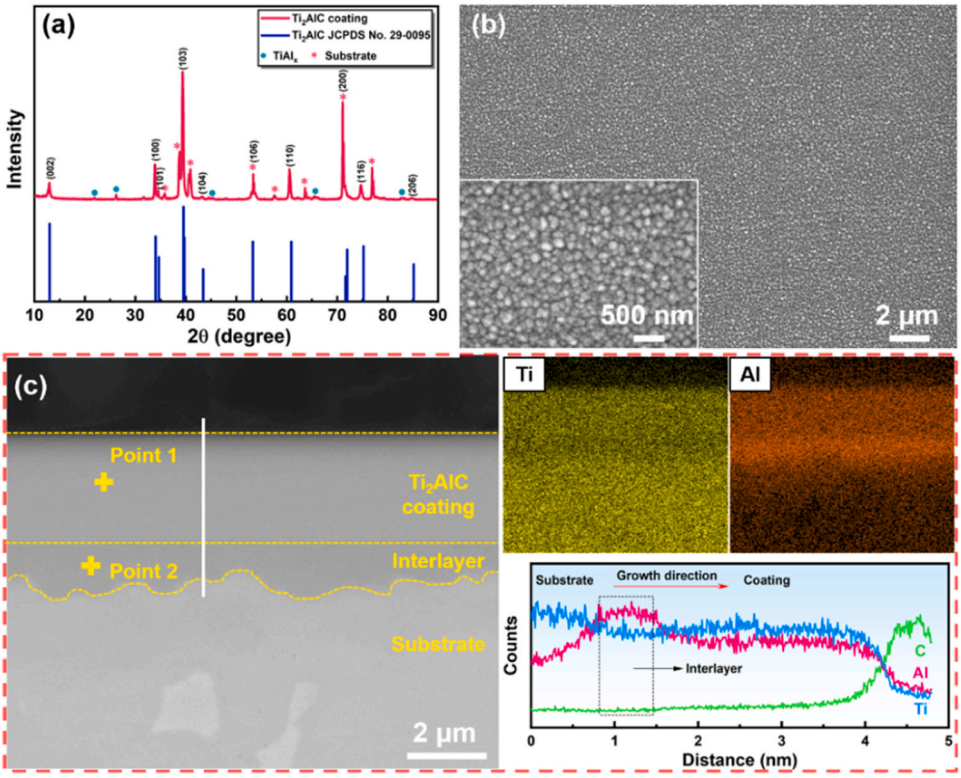

Fig. 2. (a) XRD pattern recorded from the as-prepared Ti_2AlC coating; (b) Surface morphologies of the as-deposited Ti_2AlC coating; (c) cross-sectional morphology, corresponding line-scanning results of Ti (blue), Al (rosiness) and C (green) along the marked white line and element mapping of Ti and Al.

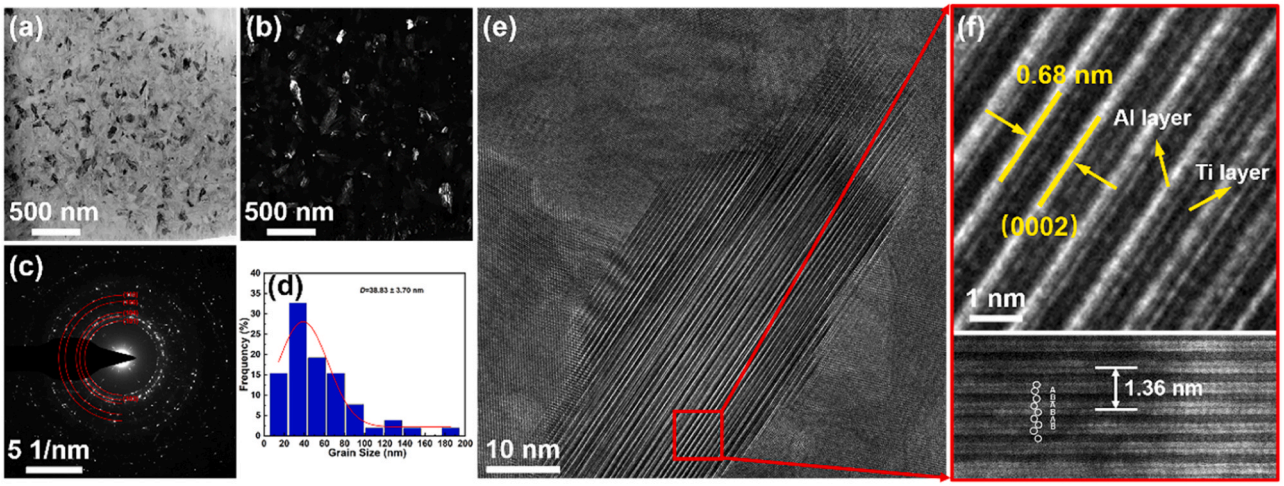

Fig. 3. (a) Cross-sectional bright-field and (b) dark-field plan-view TEM images of the as-prepared Ti_2AlC coating; (c) the selected area electron diffraction (SAED) pattern; (d) corresponding statistical histogram of the Ti_2AlC grain size calculated by the result in b; (e, f) HRTEM images and the atomic arrangement STEM image of the Ti_2AlC grain.

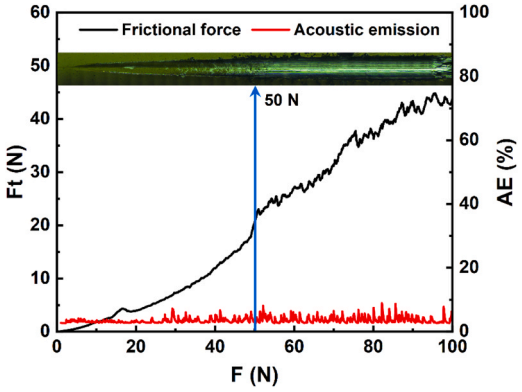

Fig. 4. The adhesion strength of the as-prepared Ti_2AlC coating on the Ti-6Al-4V substrate.

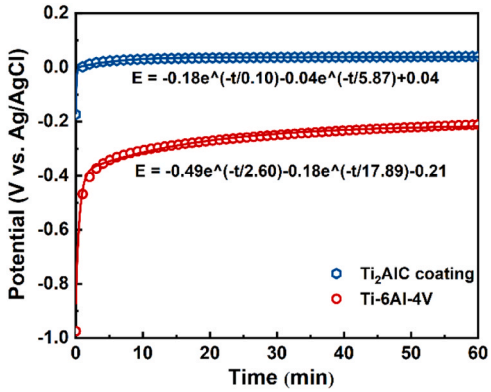

Fig. 5. E_{OCP}-time plots for Ti_2AlC coating and uncoated Ti-4Al-4V in 3.5 wt.% NaCl solution.

on the Ti-6Al-4V substrate obtained by the scratch tester with a progressive load. With increasing the load to 30 N, several acoustic emission (AE) signals were visible for the coating, suggesting the appearance of coating cracks. At a load about 50 N, a great number of strong AE signals were acquired. In parallel, the in-situ scratch morphology (insert in Fig. 4) revealed that the coating was peeled off obviously from the substrate with an exposure of pristine substrate. Therefore, it could be identified that the coating displayed a high adhesion strength of about 50 N on the Ti-6Al-4V substrate.

3.2. Electrochemical properties

3.2.1. Open circuit potential

The E_{OCP} vs. immersion time curve can generally reflect the surface variation of a specimen in contact with an etchant, in which the thermodynamic properties and electrochemical reaction kinetics can be extracted [36]. Fig. 5 presents the E_{OCP} evolution of the Ti_2AlC MAX phase coating immersed in 3.5 wt.% NaCl solution for 60 min. The same test was also conducted for the uncoated substrate for comparison. All the curves exhibited a similar trend, where the E_{OCP} shifted rapidly towards the positive value at the initial period and then gradually reached a quasi-stationary value. This stabilized value was defined as the free corrosion potential, associating with the completion of stabilized spontaneous passivation in passivated metals or alloys typically [37]. The reason behind this phenomenon could be understood from two aspects. Firstly, the initial increase in E_{OCP} arose from the immediate formation of the spontaneous protective oxide films on the exposed surface of tested specimens. Then, the dissolution of the anode workpiece was prevented, leading to a substantially positive shift in E_{OCP} values [38]. Secondly, the dynamic equilibrium between dissolution and growth of oxide film ultimately led to a relatively steady state [39,40], representing the establishment of stabilized electrochemical passive films. As shown in Fig. 5, the E_{OCP}-time curves could be fitted using an exponential decay function with two-time constants, indicating two distinct stages on the sample surface during immersion. According to the fitted results, the first-time constant was within 3 min, referring to the growth of oxide films. However, the second-time constant increased several times to 5–20 min, representing the thickening of the passive films. Apparently, the first-time constant of the coating (0.1 min) was much shorter than that of uncoated Ti-6Al-4V (2.6 min), indicating the faster growth rate of the passive film. This could be mainly ascribed to the rapid diffusion of unique nano-laminar structure in the MAX phases. Besides, the final stable E_{OCP} value of the Ti_2AlC coating was very positive, implying the spontaneous passive film formed on its surface with higher thermodynamic stability.

3.2.2. Electrochemical impedance spectroscopy

EIS measurements were performed on the Ti_2AlC coating and the uncoated Ti-6Al-4V at the stabilized E_{OCP} value after immersion for 1 h in 3.5 wt.% NaCl solution. As shown in Fig. 6, the representative results

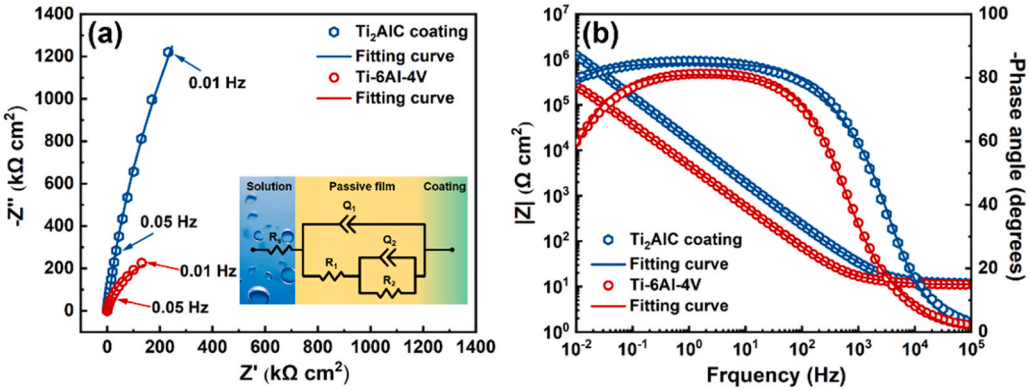

Fig. 6. (a) Nyquist plots and (b) Bode plots of Ti_2AlC coating and uncoated Ti-6Al-4V at respective open circuit potentials in 3.5 wt.% NaCl solution. The inset in (a) is the equivalent electrical circuit (EEC) used to fit the impedance spectra.

of Nyquist and Bode plots for the coating and the uncoated substrate suggested similar features in the corrosion behavior. In particular, each obtained Nyquist plot presented an unfinished capacitive loop (Fig. 6a), showing the dependence of loop radius on the absolute impedance [41]. Furthermore, the Ti_2AlC coating displayed a much higher radius of the capacitance loop and Z''/Z' ratio than those of uncoated Ti-6Al-4 V substrate. This indicated excellent electrochemical corrosion resistance with enhanced capacitive behavior for the solid/liquid interface in the Ti_2AlC coating. According to the Bode plots in Fig. 6b, a typical feature of passive materials behaving in two distinct regions appeared clearly. Within a wide range of medium- and low-frequencies, the values of log |Z| and log f were addressed as a linear relationship with a slope close to -1, corresponding to a broad phase-plateau with the phase angle approaching $-90°$ in the Bode-phase versus frequency curves. Such highly capacitive behavior could be predominantly controlled by the stable passive film formed on the specimen surface [42]. The coating displayed the broader phase angle plateau and larger phase angle maximum, simultaneously with an order of magnitude improved impedance modulus at the low-frequency limit ($|Z|_{f\to 0}$), indicating the formed passive film was more insulating and protective than that observation of substrate. At higher frequencies (5–100 kHz), the phase angle approached nearly 0°, indicating the current response was no longer lagging behind the potential change. In this range, the impedance magnitude was relatively lower and almost frequency-independent, representing a solution resistance response.

To further quantify the electrochemical properties of coating, the measured EIS spectra have been usually analyzed and best-fitted using the electrical equivalent circuits. Two of the most widely used schematics applied for passivated materials are $R_s(Q_1R_1)$ and $R_s(Q_1(R_1((Q_2R_2))))$ [43]. As presented in Fig. 6b, two overlapped time constants corresponding to the phase maxima in the medium- and low-frequency regions were revealed due to the asymmetry of Bode-phase plots. Each time constant was relevant to a parallel circuit, indicating two different relaxation processes. Consequently, the second circuit model (an inset in Fig. 6a) was selected to simulate the experimental impedance data obtained from the tested specimens. In this circuit, R_s represents the solution resistance. The high-frequency time Q_1R_1 is related with the formed passive film, where Q_1 and R_1 refer to the capacitance and resistance of the passive film, respectively [44]. In addition, the low-frequency time constant Q_2R_2 is correlated with the charge transfer process occurring at interface of passive film-substrate interface [44]. Q_2 is the electric double-layer, and R_2 is the charge transfer resistance. Notably, the non-ideal capacitance, i.e. a more general constant phase element (CPE), was therefore adopted instead of pure capacitance because the measured capacitive response never exhibited the theoretically expected phase shift of $-90°$ for an ideal dielectric. This can be attributed to the distribution of relaxation times as a consequence of surface heterogeneity and roughness [45,46]. The impedance of a CPE could be defined as:

$$Z_{CPE} = [Q(j\omega)^n]^{-1} \quad (1)$$

Where Q is the frequency independent parameter of the CPE, $j = \sqrt{-1}$ is the imaginary number, ω is the angular frequency, and n is an exponential factor ($0 \le n \le 1$). When $n = 0$, the CPE represents pure resistance. But once $n = 1$, the CPE can be treated as an ideal capacitor with Q equal to the capacitance (C). The change of n is related to the surface roughness of the formed passive film [47]. As illustrated in Fig. 6, a perfect match between the EIS data (the scatters) and the fitting curves (the solid lines) was achieved for each spectrum, in which the chi-square (χ^2) values were about the order of 10^{-4}. This observation indicated that the proposed EEC might accurately reflect the evolution of electrochemical behavior of the tested specimens in 3.5 wt.% NaCl solution. Table 3 summarizes the obtained circuit parameters from the fitting procedures. A higher R_1 value often reflects a dense passive film and hence a better protective capability of passive film on matrix [48,49]. Compared to the pristine substrate, the higher value of R_1 demonstrated that the denser passive film was formed for Ti_2AlC coating. In addition, unlike the usually strong correlation between R and solution, the capacitance (C) value regardless of solution conditions were quite favorable to identifying the dielectric property of the passive film [50]. Thereafter, the effective capacitance (C_1) of the passive film could be calculated from Q_1 through the Hsu and Mansfeld (H – M) formula [51]:

$$C_1 = Q_1^{\frac{1}{n}}(R_1)^{\frac{1-n}{n}} \quad (2)$$

Where, the C_1 value was calculated to be 5.68 and 9.77 μF cm^{-2} for Ti_2AlC coating and substrate, respectively. As the effective capacitance was much smaller, the passive film on the coating could exhibit the superior dielectric property or insulating feature comparing with that of the Ti-6Al-4V substrate. Generally, the charge transfer resistance R_2 can reflect the corrosion rate more intimately, which is inversely proportional [52]. As illustrated in Table 3, the R_2 value of the Ti_2AlC coating was evidently larger than that of Ti-6Al-4V substrate, indicating a rather difficulty in charge transfer process for a relatively slower corrosion rate. As a result, the Ti_2AlC coating performed the better anti-corrosion capability due to the formed denser passive layer, which could retard the charge transfer process more effectively.

3.2.3. *Potentiodynamic polarization curves*

Fig. 7 presents the typical potentiodynamic polarization curves of the Ti_2AlC coating and uncoated Ti-6Al-4V substrate in 3.5 wt.% NaCl solution. Regarding the anodic branch of the curves, all specimens exhibited passivation characteristics within the analyzed potential range, without any occurrence of transpassivation. Noted that the passivation behavior was slightly different from the conventional

Table 3
Electrochemical parameters fitted form EIS data for uncoated Ti-6Al-4V and the Ti_2AlC coating at their respective open circuit potentials in 3.5 wt.% NaCl solution.

Samples	R_s $\Omega\ cm^{-2}$	Q_1 $\Omega^{-1}\ cm^{-2}\ s^n$	n_1	R_1 $\Omega\ cm^{-2}$	Q_2 $\Omega^{-1}\ cm^{-2}\ s^n$	n_2	R_2 $\Omega\ cm^{-2}$	C_1 $\mu F\ cm^{-2}$	χ^2 10^{-4}
Ti-6Al-4V	11.17	2.02×10^{-5}	0.92	11.66	2.06×10^{-5}	0.88	6.35×10^{5}	5.68	2.58
Ti_2AlC coating	12.03	8.44×10^{-6}	0.94	2.38×10^{2}	2.00×10^{-6}	0.94	1.26×10^{7}	9.77	4.22

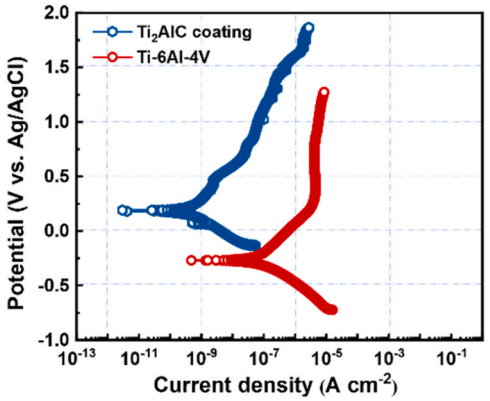

Fig. 7. Potentiodynamic polarization curves of Ti_2AlC coating and uncoated Ti-6Al-4V in 3.5 wt.% NaCl solution.

passivation featured with a decrease in current density, yet the similar phenomenon has been reported previously [30]. Specifically, the anodic branch of the polarization curve for the Ti_2AlC coating shifted downwards in current density and upwards in potential compared to the uncoated substrate. This indicated that the corrosion resistance of the coating was superior compared to that of uncoated Ti-6Al-4V. Different with the pristine substrate, moreover, the coating possessed the reduced current densities at various potential cases in the passive region distinctly. Such observations revealed the stronger electrochemical inertness of coating manifested in such a stimulated marine environment. Together with the OCP and EIS analysis above, it could thus be concluded that the passive film formed on the coating surface exhibited the superior barrier capacity, substantially enhancing the corrosion resistance of Ti-6Al-4V alloy against the heavy attack from chloride ions.

3.3. Passive film investigations

3.3.1. Stability of the passive film on Ti_2AlC coating

Further investigations were conducted for the passive film formed on the coating surface to understand the lower corrosion tendency of the Ti_2AlC coating. In particular, the passive films were generated on the surface of the Ti_2AlC coating under potentiostatic polarization at +0.2 V, +0.5 V, and +0.8 V (vs. the stable OCP) for 6 h, respectively. The EIS measurements were then carried out to evaluate the stability and evolution of the formed passive films. Fig. 8 shows the corresponding measured impedance spectra. Note that the results exhibited a similar capacitive response with an incomplete semicircle in the Nyquist plots and a phase angle close to −90° over a wide frequency range in the Bode plots, implying a typical passivation system. Compared to the EIS spectra shown in Fig. 6, all the spectra at the applied potentials presented a more pronounced capacitance loop, a broader phase plateau in the mid-frequency range and a higher impedance modulus |Z| at very low frequencies. This was identified as the truth that the passive films formed at anodic potentials owned better capacitive responses and dielectric properties. The data fitting and analysis based on Fig. 8 are listed in Table 4. At a certain polarization potential, R_1 increased by several orders of magnitude compared to that in the OCP case, where the formed passive film were compact with a good protection capability [53]. Assuming that the passive film acted as a parallel plate capacitor, the film thickness could be roughly estimated based on the following expression [54]:

$$d_p = \frac{\varepsilon_0 \varepsilon A}{C_1} \tag{3}$$

where ε_0 is the vacuum permittivity (8.854×10^{-14} F·cm^{-1}), ε is the dielectric constant of the passive film, and A refers to the exposed area (0.2 cm^2). Both the increased R_1 and the decreased C_2 indicated the increase in thickness growth for oxide films (formation rate > dissolution rate) under anodic polarization. Furthermore, when the potential reached +0.8 V, a reduction at intermediate frequency of 100 Hz was observed in the phase angle curve, accompanied by a decrease in the value of R_1 and an increase in the associated Q_1 value. This evidenced the reduction in capacitive properties and compactness [55]. Nevertheless, this degradation was very slight for ignorance, the impedance of the formed passive films could be well maintained at a higher level. For the above reasons, the formed passive film on the Ti_2AlC coating surface exhibited the remarkable stability with increased corrosion resistance under various applied potentials.

3.3.2. Chemical composition and structure of formed passive film

The chemical composition of the formed passive film has been

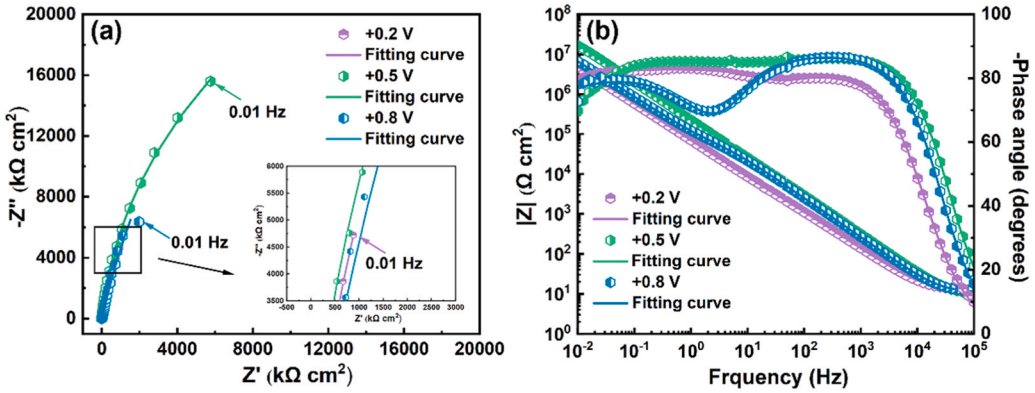

Fig. 8. (a) Nyquist plots and (b) Bode plots of the Ti_2AlC coating after potentiostatic polarization at +0.2 V, +0.5 V and +0.8 V (vs. the stable OCP) for 6 h in 3.5 wt.% NaCl solution.

Table 4
Electrochemical parameters fitted form EIS data for the Ti_2AlC coating after potentiostatic polarization at +0.2 V, +0.5 V and +0.8 V (vs. the stable OCP) for 6 h in 3.5 wt.% NaCl solution.

Samples	R_s $\Omega\ cm^{-2}$	Q_1 $\Omega^{-1}\ cm^{-2}\ s^n$	n_1	R_1 $\Omega\ cm^{-2}$	Q_2 $\Omega^{-1}\ cm^{-2}\ s^n$	n_2	R_2 $\Omega\ cm^{-2}$	C_1 $\mu F\ cm^{-2}$	χ^2 10^{-4}
Ti_2AlC coating									
+ 0.2 V	12.14	2.35×10^{-6}	0.92	2.38×10^{4}	2.72×10^{-7}	0.94	7.75×10^{7}	1.83	0.62
+ 0.5 V	9.31	6.55×10^{-7}	0.97	1.07×10^{5}	1.17×10^{-7}	0.84	6.41×10^{7}	0.60	1.22
+ 0.8 V	10.99	7.58×10^{-7}	0.97	9.85×10^{4}	1.04×10^{-6}	0.85	1.14×10^{8}	0.70	3.11

empirically observed to have a significant impact on its properties. In order to address the evolution of chemical composition and bonding state in the passive films under different applied potentials, the XPS analysis was conducted on the surface of Ti_2AlC coating after potentiostatic polarization at +0.2 V, +0.5 V, and +0.8 V (vs. the stable OCP) for 6 h, respectively. Fig. 9 shows the high-resolution spectra of Al 2p, C 1s, O 1s, and Ti 2p. No visible peaks arising from coating beneath the passive films were detected in all cases, indicating the thickness of the passive films exceeded 10 nm beyond the XPS technique [56]. After deconvolution of the C 1s core level spectra (Fig. 9a), all the peaks could be decomposed into three distinct. The asymmetric C-C bonding peak at 284.8 eV was deconvoluted to a sp^3 bond peka at 286.3 eV and a sp^2 bond peak at 284.7 eV, another peak at 288.6 eV was C═O bond [57]. These detections for carbon components could be ascribed to the inevitable surface contamination of specimens exposed to the atmosphere during preparation or acetone/ethanol cleaning. As shown in Fig. 9b and c, the spectra of Al 2p and O 1s collected from the passive films exhibited only one peak at ~74.7 eV and 531.6 eV, respectively, corresponding to the stoichiometric Al_2O_3. Moreover, the slight variations in the binding energies of Al 2p and O 1s observed under different applied potentials might be the consequence of diverse electric conductivity related to the contaminated surface. In comparison, no signal of chemical state and elemental composition was found in the spectral line of Ti 2p (Fig. 9d), indicating the absence of corrosion reaction with Ti. In this case, it could be concluded that, regardless of the potentials applied, the formed passive film was mainly composed of aluminum oxide (Al_2O_3), which was quite different from the previously observed presence of M-based oxide scale in Cr_2AlC, Ti_3AlC_2 and Ti_3SiC_2 MAX phases [58,59].

To further elucidate the chemical microstructure in the passive film on the Ti_2AlC coating, the FIB approach was employed to take a representative transverse foil containing passive film and Ti_2AlC coating from the sample polarized at +0.5 V for 6 h in 3.5 wt.% NaCl solution. Moreover, a protective carbon layer was deposited before cutting the sample to avoid damage to the oxide layer. Fig. 10 shows the cross-sectional morphologies observed by the TEM bright field, where the coating, passive film and the deposited C layer were clearly visible. The formed passive film was found to be continuous and amorphous with a homogenous thickness of 40 nm. The enlarged image in Fig. 10b demonstrated that such a passive film was also very dense and free from defects like cracks, voids or spallation. In addition, the observation of a distinct interface without any defects evidenced that there was an excellent adherent feature between the coating and the formed passive film.

Fig. 11a shows the STEM-HADDF image at the nanometer scale, in which the corresponding EDS profiles, including line scanning and elemental mapping across the passive film, were performed. As expected from the XPS results in Fig. 9, the passive film exhibited complete enrichment of Al and O elements while no trace of Ti element was detected. Meanwhile, the enriched Al and O elements were uniformly distributed in the passive film, as seen in the EDS mapping image, demonstrating only a formed single-layer structure with Al oxides. Most importantly, the concentration of O decreased significantly to a very low level at the interface between the coating and the passive film. It was therefore suggested that the dense and continuous passive film acting as a barrier suppressed the further corrosion to the inside of the coating. Supporting evidence was that, beyond the topmost contaminated C layer, the surface film consisted mainly of Al and O elements with no Ti and C present (XPS depth profiles in Fig. 11b). Furthermore, the concentration of Al and O, with an atomic ratio of 2/3, remained almost unchanged from the surface (20 s) to the coating (> 500 s), which was in line with the stoichiometric ratio of Al_2O_3. After etching for 600 s, the composition of the Ti_2AlC coating was discernible through a slight increase in the Ti and C contents in parallel with the decrease in Al and O. However, it was interesting to note that the passive film was not completely etched at this point, and the atomic ratio of Al and O was still maintained at about 2/3. Therefore, it was believed that, under anodic polarization in NaCl solution, the passive film covered on the Ti_2AlC coating was the compact and continuous Al_2O_3 with amorphous characteristics, without other corrosion products and obvious layered distributions. These experimental results suggested that the anodic oxidation of the Ti_2AlC coating exposed to NaCl solution was chemically selective rather than homogenously inclusive.

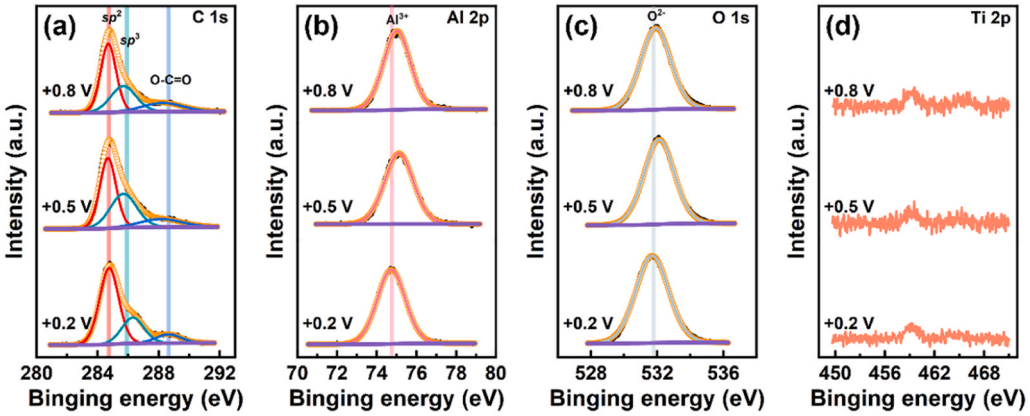

Fig. 9. High resolution XPS spectra of (a) Al 2p, (b) O 1s, (c) C 1s and (d) Ti 2p on the surface of the Ti_2AlC coating after potentiostatic polarization at +0.2 V, +0.5 V and +0.8 V (vs. the stable OCP) for 6 h.

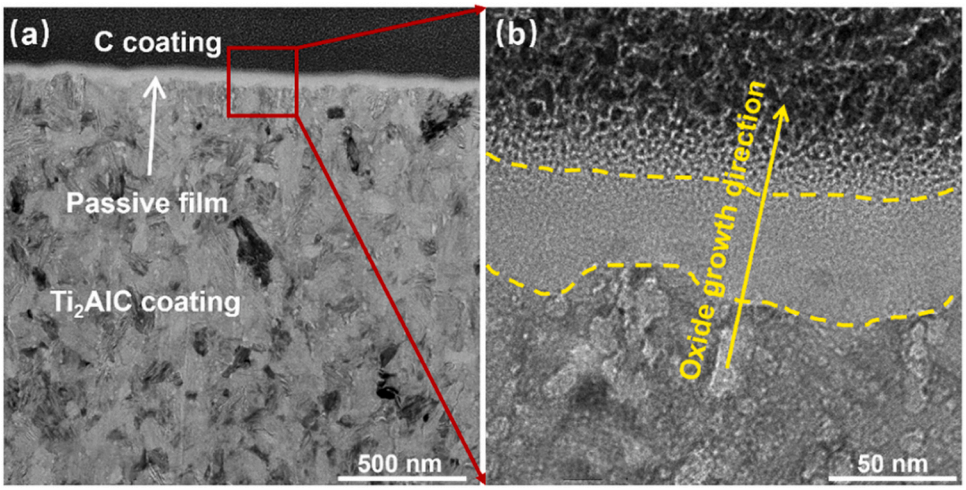

Fig. 10. TEM bright images at low (a) and high (b) magnification of the passive film formed on the Ti_2AlC coating.

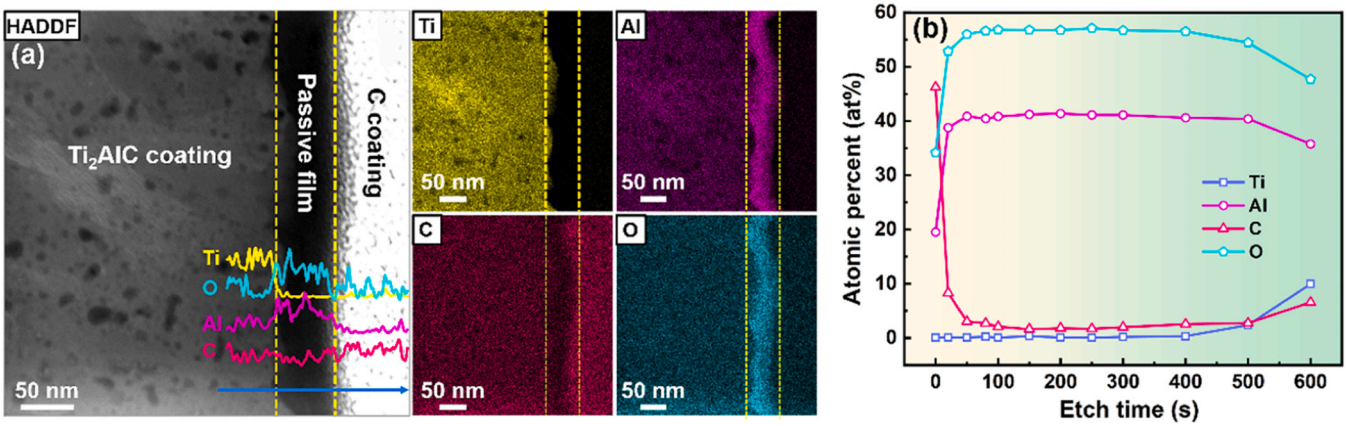

Fig. 11. (a) STEM-HAADF images of the transvers foil of the sample polarized at +0.5 V for 6 h in 3.5 wt.% NaCl solution, corresponding line-scanning profiles of Ti, Al, C and O elements along the blue arrow, and Ti (yellow), Al (purple), C (pink) and O (sky-blue) elemental maps; (b) depth profiles of Ti, Al, C and O concentration on the surface of the Ti_2AlC coating after potentiostatic polarization at +0.5 V for 6 h in 3.5 wt.% NaCl solution.

3.3.3. *Mott-Schottky analysis*

Passive films formed on most metals or alloys often exhibit semiconducting behavior, which can be described by Mott-Schottky analysis. Fig. 12a and b display the Mott-Schottky plots for the passive films formed on the Ti_2AlC coating and un-coated Ti-6Al-4V substrate after potentiostatic polarization at +0.2 V, +0.5 V, and +0.8 V (vs. the stable OCP) for 6 h in the 3.5 wt.% NaCl solution, respectively. The results suggested the presence of a break point that separated the Mott-Schottky plots into two liner regions at low and high potentials over the entire potential range, corresponding to the semiconducting and dielectric behavior of the passive films, respectively [60]. Moreover, the slopes of two linear regions in each plot were always positive, demonstrating the n-type semiconducting property of the passive films formed on both the substrate and coating. The M-S relationship for n-type semiconductor can be expressed as:

$$\frac{1}{C^2} = \frac{2}{\varepsilon\varepsilon_0 e N_D}\left(E - E_{fb} - \frac{kT}{e}\right) \tag{4}$$

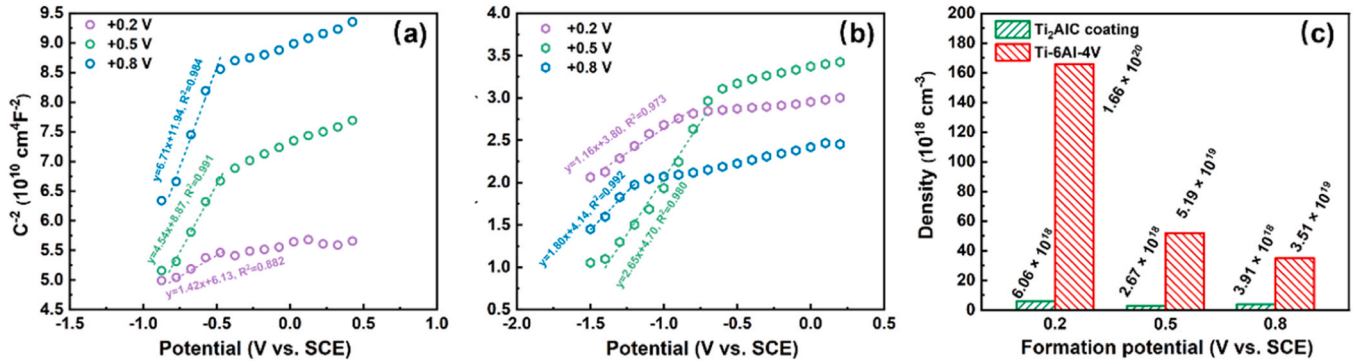

Fig. 12. Mott-Schottky plots of the passive films formed at +0.2 V, +0.5 V and +0.8 V (vs. the stable OCP) for 6 h in 3.5 wt.% NaCl solution.

where ε is the dielectric constant of the passive film (usually taken as 60 for TiO_2 and 10 for Al_2O_3), ε_0 is the vacuum permittivity (8.854×10^{-12} F/m), e is the charge of the electron (1.602×10^{-19} C), N_D represents the donor density, E_{fb} is the flat band potential, k is the Boltzmann constant (1.38×10^{-23} J/K) and T is the absolute temperature (298 K). In the case of n-type passive films, the primary donors are O vacancies in the oxide. According to the point defect model (PDM), the migration of O vacancies across the passive film governs the whole electrochemical process. This is because negatively charged chloride ions tend to occupy positively charged oxygen vacancies in the passive film [61]. Therefore, a higher N_D implies a higher ion conductivity of the passive film. In other words, an excessive number of donors would deteriorate the properties of the passive film.

The calculated donor density for the passive films formed at different potentials, as shown in Fig. 12c, was obtained from Mott-Schottky plots. When the potential was increased from +0.2 V to +0.8 V, the N_D of the passive films for the coating initially decreased and reached the lowest value at +0.5 V. It then slightly increased at +0.8 V, which was consistent with the EIS results. This suggested that the evolution of the passive film involved changes in ionic defects within the oxide, i.e., the film became more defective at higher potential. However, at the same film formation potential, the N_D values of the coating were all lower than those of Ti-6Al-4V sample. They exhibited a reduction by one or two orders of magnitude. Taking the results into consideration, it is reasonable to conclude that the passive film formed on the Ti_2AlC coating was more compact and had reduced defectiveness, thereby increasing its corrosion resistance.

3.4. Formation mechanism of the passive film

As mentioned above, the passivation layer formed on the Ti_2AlC coating in NaCl solution was dense pure amorphous Al_2O_3, which favored the enhancement of the corrosion resistance of the coated Ti-6Al-4V alloy. To further indicate the evolution of the passive films, the chemical compositions dissolved in the aqueous solutions were analyzed using ICP-OES after the potentiostatic polarization tests, where the initial solutions were diluted ten times to satisfy the measurement. Table 5 illustrates the changes in composition for the Ti and Al elements in various polarization situations. Regardless of the potentials applied, the concentrations of both Ti and Al in the solution after potentiostatic polarization were found to be almost undetectable, approaching a negligible level of 0 mg/L. Combined with the above discussion in Section 3.3.2, it was therefore speculated that, during the polarization process, only the intercalated Al element within the Ti_2AlC MAX phase continuously diffused outwards to the coating surface and participated in the formation of corrosive oxidized products, rather than dissolving into the solution.

In fact, Marcus proposed that both Ti and Al were defined as passivity promoters [62], possessing equilibrium oxidation potentials well below the reduction of water. When exposed to most aqueous solutions, both Ti and Al strongly tend to combine with either O^{2-} or OH^- ions. Considering the oxidation difference between aqueous solutions and pure oxygen, the TiO_2 phase was preferentially generated in the oxygen case [63]. In other words, the oxidation process in solutions was not only determined by thermodynamic reactions related to the standard Gibbs free energy of formation. Specifically, the growth of the anodic passive film generally occurs at the metal/electrolyte interface, and the migration of metallic elements is considered to be the most crucial factor influencing the rendered oxide species in the passive film [64]. Based on many studies on MAX phases [58,59], the A element is more likely to slip out from the MAX phase cell due to the layered crystal structure and the weaker chemical bond between A and MX layers. The vacancy-mediated diffusion and the related mechanism could be imperatively discussed to understand this kinetic behavior of MAX phases. The vacancy formation energy in Ti_2AlC was defined by the following equation [65]:

$$\Delta E_v = E_{defect} - E_{perfect} + \mu_i \tag{5}$$

Where the E_{defect} is the total energy of a supercell with an atom vacancy, $E_{perfect}$ is the energy of a defect-free supercell, while μ_i is the chemical potential of each species approximated by the average atomic energy of the solid used. Fig. 13a displays the vacancy formation energies of each species in different supercells of Ti_2AlC, which were calculated around 5.619 eV, 2.796 eV and 7.692 eV for Ti, Al and C mono-vacancies, representing a sequence of $\Delta E_v^C > \Delta E_v^{Ti} > \Delta E_v^{Al}$. Comparatively, the Al vacancy was the most energetically favorable mono-vacancy in the defective Ti_2AlC structure. Afterwards, the migration of each atom was simulated for the changes in diffusion energy (Fig. 13b). It could be visible that the diffusion energy barrier of Al atom in the Ti_2AlC phase was as low as 0.901 eV, which was much lower than that for Ti and C. The simulations favored the establishment of a correlation between the atomic mobility and the passive film formed on the Ti_2AlC coating, showing that the Al atom would yield higher mobility in Ti_2AlC by reducing the formation and migration energies, thereby allowing the Al element to preferentially capture oxygen to form the passive film of the Al oxides in the Ti_2AlC coating.

On the other hand, the depletion of Al via out-diffusion might induce the unstable and experience decomposition for MAX phases, which in turn affects the oxidation/passivation behavior at the later stage. In this case, the difference of cohesive energy ΔE_{coh} at various Al contents was also calculated to evaluate the stability of defective Ti_2Al_xC (with Al vacancies). Specifically, the crystal structures with different Al vacancies were represented by a $2 \times 2 \times 1$ supercell after removing various Al atoms. The difference of cohesive energy ΔE_{coh} at various Al vacancies was calculated by:

$$\Delta E_{coh} = E_{coh}^{\text{defect}} - 2E_{coh}^{TiC_{0.5}} - xE_{coh}^{Al} \tag{6}$$

where E_{coh}^{defect}, $E_{coh}^{Ti_2C}$ and E_{coh}^{Al} are the cohesive energies of Ti_2AlC with Al vacancies, Ti_2C and Al atom, respectively; while x is assigned to the content of Al in defect structures. A positive ΔE_{coh} indicates the phase is sustained, while a negative value suggests the phase decomposition or instability. Fig. 13c plots the calculated cohesive energy for the Ti_2AlC phase at different Al vacancies. As Al vacancies increased, the cohesive energy difference continuously decreased and the energy difference value remained positive until the Al vacancy reached approximately 0.5. Beyond the critical value, the energy changed from positive to negative, suggesting that the phase tended to be unstable. All these achievements demonstrated that the defective Ti_2Al_xC could maintain the phase stability well even after consuming half of the Al content in the structure.

An example of the interface between the Ti_2AlC coating and the formed Al_2O_3 passive layer after potentiostatic polarization at +0.5 V in 3.5 wt.% NaCl solution is shown in Fig. 14. As can be seen in Fig. 14a, the crystal grains adjacent to the Al_2O_3 layer remained the plate-like feature with a large aspect ratio, consistent with the corrosion-free grain structure in Fig. 3e~f. Furthermore, according to the enlarged image (Fig. 14b) from the red marked area in Fig. 14a, the Fast Fourier Transform (FFT) indicated that the planar spacing of the localized individual grain was about 0.23 nm, corresponding to the (103) orientation of the Ti_2AlC MAX phase. Together with the SAED pattern (Fig. 14c), the hexagonal Ti_2AlC phase was indexed along the $[11\bar{2}0]$ zone axis. Therefore, it was clear that the Ti_2AlC coating beneath the

Table 5
Chemical compositions of aqueous solutions determined by ICP-MS after potentiostatic polarization at +0.2 V, +0.5 V and +0.8 V (vs. the stable OCP) for 6 h in 3.5 wt.% NaCl solution.

	+0.2 V-6 h	+0.5 V-6 h	+0.8 V-6 h
Ti (mg/L)	< 0.002	< 0.001	< 0.002
Al (mg/L)	< 0.008	< 0.003	< 0.002

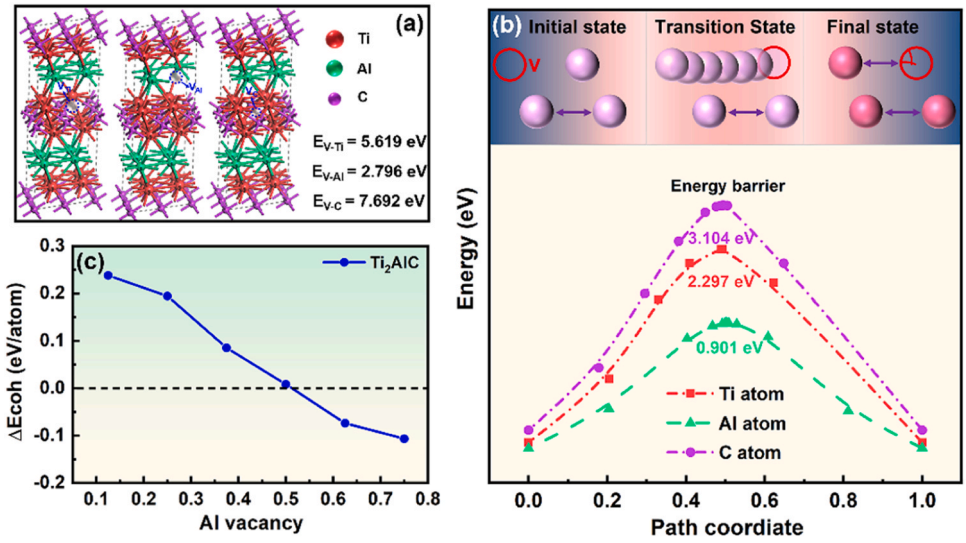

Fig. 13. (a) The formation energy of a mono-vacancy in Ti_2AlC MAX phase; (b) migration energy of atoms in Ti_2AlC MAX phase; (c) cohesive energy for Ti_2AlC phase at different Al vacancy.

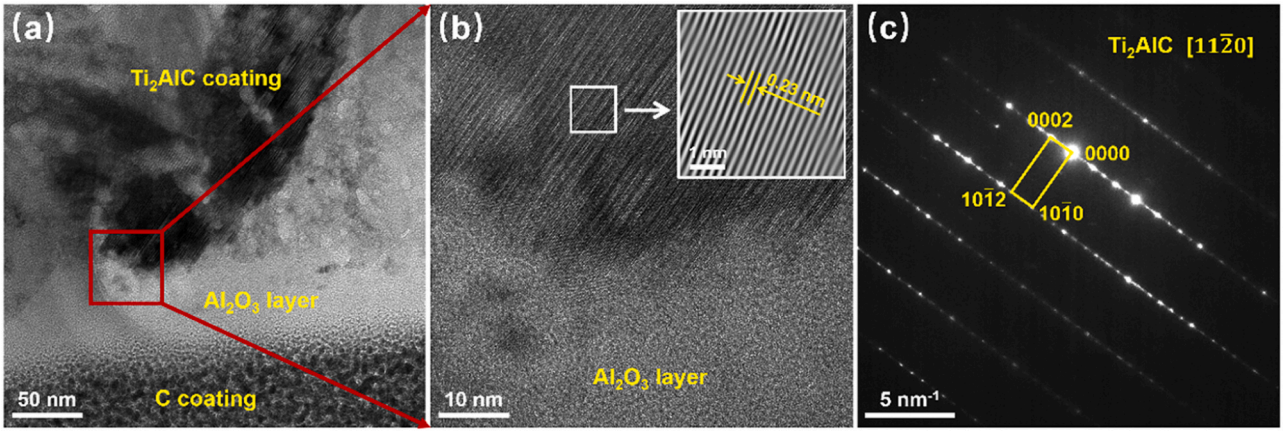

Fig. 14. (a) HRTEM image of the transvers foil of the sample polarized at +0.5 V for 6 h in 3.5 wt.% NaCl solution; (b) locally enlarged image at the interface between the passive film and the Ti_2AlC coating; (c) corresponding SAED patterns with the electron beam parallel to the [11$\bar{2}$0] direction.

Al_2O_3 layer sustained both phase and structural stability even when a significant amount of Al was depleted.

To conclude the discussion on the evolution of the passive film in Ti_2AlC coating under NaCl solution, the corrosion mechanism could be understood in principle from the two aspects shown in Fig. 15. Firstly, the unique nano-laminated structure of Ti_2AlC MAX phase coating resulted in strong preferential oxidation of Al element over Ti when exposed to 3.5 wt.% NaCl solution, which was very different from the similar passivity promoters for Ti and Al with the equilibrium potentials of oxidation far below the reduction of water. The atomic simulation indicated that the higher mobility of the Al atom in the Ti_2AlC system favored the excellent capability to capture oxygen preferentially, subsequently forming the passive film of dense Al oxides on the coating surface. Most importantly, the interesting result suggested that the defective Ti_2Al_xC structure still showed excellent phase stability even though half of the Al content in the Ti_2AlC coating was consumed. This contributed significantly to the formation of pure Al_2O_3 passive film with dense, continuous and amorphous characteristics covering the coating surface, which could remain stable at anodic polarization up to +0.8 V. The aforementioned observations collectively contributed to the superior corrosion resistance exhibited by the Ti_2AlC MAX phase coating in a 3.5 wt.% NaCl solution, thereby presenting a promising protective strategy for mechanical components employed in demanding marine environments.

4. Conclusions

In summary, we have successfully fabricated the high-purity and dense Ti_2AlC MAX phase coating with unique equiaxial grains on the Ti-6Al-4V substrate using a hybrid two-step method, which was particularly composed of the multi-target HiPIMS technique and the subsequent vacuum annealing. The comprehensive experiments and DFT calculations were conducted to elucidate the dependence of electrochemical behavior upon the microstructural evolution of the Ti_2AlC coating exposed to the stimulated 3.5 wt.% NaCl solution. The main conclusions could be deduced as follows:

(1) The potentiodynamic polarization and EIS analysis revealed that the corrosion resistance of the pristine Ti-6Al-4V substrate was significantly improved by applying Ti_2AlC MAX phase coating, as evidenced by a distinct reduction in current densities and a large increase in impedance value.
(2) On the basis of XPS and TEM studies, the passive film formed on the Ti_2AlC coating was mainly dominated by single Al_2O_3 with

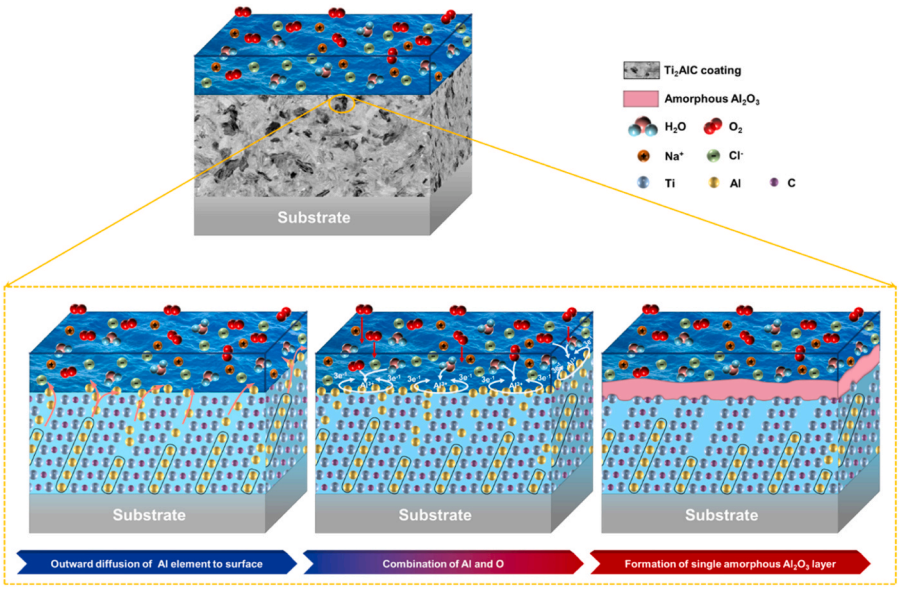

Fig. 15. Schematic diagram showing the passivation mechanism and process of Ti_2AlC coating in 3.5 wt.% NaCl solution.

continuous compact and amorphous characteristics, which favored the outstanding stability and the stronger resistance over a wide range with applied potentials.

(3) The Mott-Schottky studies evidenced that the passive film formed on the Ti_2AlC coating exhibited n-type semiconductor behavior with a donor density around 10^{18} cm^{-3}, which was far less than that for the passive film generated on the pristine Ti-6Al-4V substrate.

(4) The reason behind of the remarkable passivation capability and superior corrosion resistance of the Ti_2AlC coating could be understood from two aspects. Firstly, the Ti_2AlC coating indicated the higher transport kinetics for Al atoms than Ti atoms, which benefited the preferential formation of the passive layer of Al_2O_3 film. Most importantly, another reason could be that the stronger tolerance for Al vacancies over 50% favored the stabilized defective Ti_2Al_xC structure with consumed Al elements.

Consequently, the presented observations not only identified the electrochemical evolution and corrosion mechanism of Ti_2AlC coating in simulated seawater medium, but also provided the promising strategy to utilize these MAX phase coatings for the required protective application over a wide range of harsh corrosive environments.

CRediT authorship contribution statement

Ma Guanshui: Visualization, Software. **Ke Peiling:** Supervision. **Wang Aiying:** Writing – review & editing, Supervision, Funding acquisition, Conceptualization. **Li Zhongchang:** Writing – original draft, Investigation, Data curation. **Zhang Yan:** Investigation. **Wang Kaihang:** Methodology. **Wang Zhenyu:** Writing – review & editing, Supervision.

Declaration of Competing Interest

The authors declare that they have no known competing financial interests or personal relationships that could have appeared to influence the work reported in this paper.

Data availability

Data will be made available on request.

Acknowledgments

The work was financially supported by the National Science Fund for Distinguished Young Scholars of China (52025014), the National Natural Science Foundation of China (U22A20111, 52171090), the Youth Innovation Promotion Association CAS (2023312), and the Natural Science Foundation of Ningbo (2023J410).

References

[1] M. Keddam, S. Taktak, Characterization and diffusion model for the titanium boride layers formed on the Ti6Al4V alloy by plasma paste boriding, Appl. Surf. Sci. 399 (2017) 229–236.
[2] X.-B. Liu, X.-J. Meng, H.-Q. Liu, G.-L. Shi, S.-H. Wu, C.-F. Sun, M.-D. Wang, L.-H. Qi, Development and characterization of laser clad high temperature self-lubricating wear resistant composite coatings on Ti–6Al–4V alloy, Mater. Des. 55 (2014) 404–409.
[3] Y.S. Tian, C.Z. Chen, S.T. Li, Q.H. Huo, Research progress on laser surface modification of titanium alloys, Appl. Surf. Sci. 242 (2005) 177–184.
[4] C. Fei, Z. Yulin, L. Weiguang, F. Wenran, Y. Yingge, Corrosion behavior of W-Mo Co-penetrated layer produced by glow discharge plasma technique in acid solution, Rare Met. Mater. Eng. 47 (2018) 723–728.
[5] Y. Zhang, F. Chen, Y. Zhang, Z. Liu, X. Wang, C. Du, Influence of graphene oxide on the antiwear and antifriction performance of MAO coating fabricated on Mg Li alloy, Surf. Coat. Technol. 364 (2019) 144–156.
[6] K.S. Zhou, H. Herman, Cavitation erosion of titanium and Ti-6Al-4V: effects of nitriding, Wear 80 (1982) 101–113.
[7] J. Feng, J. Wang, K. Yang, J. Rong, Microstructure and performance of $YTaO_4$ coating deposited by atmospheric plasma spraying on TC4 titanium alloy surface, Surf. Coat. Technol. 431 (2022).
[8] Y. Fu, B. Yan, N.L. Loh, C.Q. Sun, P. Hing, Characterization and tribological evaluation of MW-PACVD diamond coatings deposited on pure titanium, Mater. Sci. Engine A 282 (2000) 38–48.
[9] D. Nolan, S.W. Huang, V. Leskovsek, S. Braun, Sliding wear of titanium nitride thin films deposited on Ti–6Al–4V alloy by PVD and plasma nitriding processes, Surf. Coat. Technol. 200 (2006) 5698–5705.
[10] F. Yildiz, A.F. Yetim, A. Alsaran, A. Çelik, Plasma nitriding behavior of Ti6Al4V orthopedic alloy, Surf. Coat. Technol. 202 (2008) 2471–2476.
[11] Y.-Z. Xing, C.-P. Jiang, J.-M. Hao, Time dependence of microstructure and hardness in plasma carbonized Ti–6Al–4V alloys, Vacuum 95 (2013) 12–17.
[12] V. Totolin, V. Pejaković, T. Csanyi, O. Hekele, M. Huber, M. Rodríguez Ripoll, Surface engineering of Ti6Al4V surfaces for enhanced tribocorrosion performance in artificial seawater, Mater. Des. 104 (2016) 10–18.
[13] A. Krella, An experimental parameter of cavitation erosion resistance for TiN coatings, Wear 270 (2011) 252–257.
[14] J. Xu, W. Hu, Z.-H. Xie, P. Munroe, Reactive-sputter-deposited β-Ta_2O_5 and TaON nanoceramic coatings on Ti–6Al–4V alloy against wear and corrosion damage, Surf. Coat. Technol. 296 (2016) 171–184.
[15] A.P. Serro, C. Completo, R. Colaço, F. dos Santos, C.L. da Silva, J.M.S. Cabral, H. Araújo, E. Pires, B. Saramago, A comparative study of titanium nitrides, TiN, TiNbN and TiCN, as coatings for biomedical applications, Surf. Coat. Technol. 203 (2009) 3701–3707.

[16] J. Xu, S. Peng, Z. Li, S. Jiang, Z.H. Xie, P. Munroe, The influence of semiconducting properties of passive films on the cavitation erosion resistance of a NbN nanoceramic coating, Ultrason Sonochem. 71 (2021) 105406.
[17] M.W. Barsoum, The $M_{n+1}AX_n$ phases: a new class of solids; thermodynamically stable nanolaminates, Prog. Solid State Chem. 28 (2000) 201–281.
[18] Q. Tao, J. Lu, M. Dahlqvist, A. Mockute, S. Calder, A. Petruhins, R. Meshkian, O. Rivin, D. Potashnikov, Ea.N. Caspi, H. Shaked, A. Hoser, C. Opagiste, R.-M. Galera, R. Salikhov, U. Wiedwald, C. Ritter, A.R. Wildes, B. Johansson, L. Hultman, M. Farle, M.W. Barsoum, J. Rosen, Atomically layered and ordered rare-earth i-MAX phases: a new class of magnetic quaternary compounds, Chem. Mater. 31 (2019) 2476–2485.
[19] Z.M. Sun, Progress in research and development on MAX phases: a family of layered ternary compounds, Int. Mater. Rev. 56 (2013) 143–166.
[20] P. Eklund, M. Beckers, U. Jansson, H. Högberg, L. Hultman, The $M_{n+1}AX_n$ phases: materials science and thin-film processing, Thin Solid Films 518 (2010) 1851–1878.
[21] Z. Feng, P. Ke, Q. Huang, A. Wang, The scaling behavior and mechanism of Ti_2AlC MAX phase coatings in air and pure water vapor, Surf. Coat. Technol. 272 (2015) 380–386.
[22] Z. Wang, J. Sun, B. Xu, Y. Liu, P. Ke, A. Wang, Reducing the self-healing temperature of Ti_2AlC MAX phase coating by substituting Al with Sn, J. Eur. Ceram. Soc. 40 (2020) 197–201.
[23] Z. Wang, G. Ma, Z. Li, H. Ruan, J. Yuan, L. Wang, P. Ke, A. Wang, Corrosion mechanism of Ti_2AlC MAX phase coatings under the synergistic effects of water vapor and solid NaCl at 600 °C, Corros. Sci. 192 (2021).
[24] J. Cao, Z. Yin, H. Li, G. Gao, X. Zhang, Tribological and mechanical properties of Ti_2AlC coating at room temperature and 800 °C, Ceram. Int. 44 (2018) 1046–1051.
[25] Z. Wang, W. Li, Y. Liu, J. Shuai, P. Ke, A. Wang, Diffusion-controlled intercalation approach to synthesize the Ti_2AlC MAX phase coatings at low temperature of 550 °C, Appl. Surf. Sci. 502 (2020).
[26] Y. Li, G. Zhao, Y. Qian, J. Xu, M. Li, Deposition and characterization of phase-pure Ti_2AlC and Ti_3AlC_2 coatings by DC magnetron sputtering with cost-effective targets, Vacuum 153 (2018) 62–69.
[27] J. Alami, S. Bolz, K. Sarakinos, High power pulsed magnetron sputtering: fundamentals and applications, J. Alloy. Compd. 483 (2009) 530–534.
[28] Z. Li, G. Zhou, Z. Wang, J. Yuan, P. Ke, A. Wang, HiPIMS induced high-purity Ti3AlC2 MAX phase coating at low-temperature of 700 °C, J. Eur. Ceram. Soc. 43 (2023) 4673–4683.
[29] A. Anders, J. Andersson, A. Ehiasarian, High power impulse magnetron sputtering: current-voltage-time characteristics indicate the onset of sustained self-sputtering, J. Appl. Phys. 102 (2007).
[30] Z.B. Zheng, Y.G. Zheng, W.H. Sun, J.Q. Wang, Effect of applied potential on passivation and erosion–corrosion of a Fe-based amorphous metallic coating under slurry impingement, Corros. Sci. 82 (2014) 115–124.
[31] Z.-C. Zhang, A.-D. Lan, M. Zhang, J.-W. Qiao, Effect of Ce on the pitting corrosion resistance of non-equiatomic high-entropy alloy Fe40Mn20Cr20Ni20 in 3.5wt% NaCl solution, J. Alloy. Compd. 909 (2022).
[32] M.D. Segall, P.J.D. Lindan, M.J. Probert, C.J. Pickard, P.J. Hasnip, S.J. Clark, M. C. Payne, First-principles simulation: ideas, illustrations and the CASTEP code, J. Phys.: Condens. Matter 14 (2002) 2717–2744.
[33] J.P. Perdew, K. Burke, M. Ernzerhof, Generalized gradient approximation made simple, Phys. Rev. Lett. 77 (1996) 3865–3868.
[34] N. Govind, M. Petersen, G. Fitzgerald, D. King-Smith, J. Andzelm, A generalized synchronous transit method for transition state location, Comput. Mater. Sci. 28 (2003) 250–258.
[35] M. Ratova, G.T. West, P.J. Kelly, Optimisation of HiPIMS photocatalytic titania coatings for low temperature deposition, Surf. Coat. Technol. 250 (2014) 7–13.
[36] A.A. Hermas, M.S. Morad, A comparative study on the corrosion behaviour of 304 austenitic stainless steel in sulfamic and sulfuric acid solutions, Corros. Sci. 50 (2008) 2710–2717.
[37] I. Milošev, G. Žerjav, J.M. Calderon Moreno, M. Popa, Electrochemical properties, chemical composition and thickness of passive film formed on novel Ti–20Nb–10Zr–5Ta alloy, Electrochim. Acta 99 (2013) 176–189.
[38] E. Nouicer, F.Z. Benlahreche, L. Yahia, M. Eutamene, H. Chadli, Effect of scan rates and imposed potentials on the formation and growth of oxide film on Ti6Al4V alloy surface in 3% NaCl, Rev. De. Métall. 108 (2011) 69–74.
[39] Y.-K. Wei, Y.-J. Li, Y. Zhang, X.-T. Luo, C.-J. Li, Corrosion resistant nickel coating with strong adhesion on AZ31B magnesium alloy prepared by an in-situ shot-peening-assisted cold spray, Corros. Sci. 138 (2018) 105–115.
[40] M. Daroonparvar, M.U. Farooq Khan, Y. Saadeh, C.M. Kay, R.K. Gupta, A.K. Kasar, P. Kumar, M. Misra, P.L. Menezes, H.R. Bakhsheshi-Rad, Enhanced corrosion resistance and surface bioactivity of AZ31B Mg alloy by high pressure cold sprayed monolayer Ti and bilayer Ta/Ti coatings in simulated body fluid, Mater. Chem. Phys. 256 (2020).
[41] J. Xu, J. Cheng, S. Jiang, P. Munroe, Z.-H. Xie, The influence of Ti additions on the mechanical and electrochemical behavior of β-Ta5Si3 nanocrystalline coating, Appl. Surf. Sci. 419 (2017) 901–915.
[42] A.M. Fekry, R.M. El-Sherif, Electrochemical corrosion behavior of magnesium and titanium alloys in simulated body fluid, Electrochim. Acta 54 (2009) 7280–7285.
[43] J. Xu, L. Liu, P. Munroe, Z.-H. Xie, Z.-T. Jiang, The nature and role of passive films in controlling the corrosion resistance of MoSi2-based nanocomposite coatings, J. Mater. Chem. A 1 (2013).
[44] X. Liu, S. Chen, J. Zhang, G. Yang, Y. Zhang, T. Wang, J. Lei, Enhancement of the electrochemical corrosion resistance of Ti6Al4V alloy reinforced by nano- and micro-TiC particles through directed energy deposition, Corros. Sci. 221 (2023).
[45] K. Jüttner, Electrochemical impedance spectroscopy (EIS) of corrosion processes on inhomogeneous surfaces, Electrochim. Acta 35 (1990) 1501–1508.
[46] X. Wang, Z. Chen, E. Guo, X. Liu, H. Kang, T. Wang, The role of Ga in the microstructure, corrosion behavior and mechanical properties of as-extruded Mg–5Sn–xGa alloys, J. Alloy. Compd. 863 (2021).
[47] C.A. Della Rovere, J.H. Alano, R. Silva, P.A.P. Nascente, J. Otubo, S.E. Kuri, Characterization of passive films on shape memory stainless steels, Corros. Sci. 57 (2012) 154–161.
[48] T. Ge, L. Chen, P. Gu, X. Ren, X. Chen, Microstructure and corrosion resistance of TiC/Inconel 625 composite coatings by extreme high speed laser cladding, Opt. Laser Technol. 150 (2022).
[49] J. Pan, D. Thierry, C. Leygraf, Electrochemical impedance spectroscopy study of the passive oxide film on titanium for implant application, Electrochim. Acta 41 (1996) 1143–1153.
[50] R.K. Potucek, R.G. Rateick Jr., V.I. Birss, Impedance characterization of anodic barrier Al oxide film beneath porous oxide layer, J. Electrochem. Soc. 153 (2006) B304–B310.
[51] C.H. Hsu, F. Mansfeld, Technical note: concerning the conversion of the constant phase element parameter Y0 into a capacitance, Corrosion 57 (2001) 747–748.
[52] M. Cao, L. Liu, Z. Yu, L. Fan, Y. Li, F. Wang, Electrochemical corrosion behavior of 2A02 Al alloy under an accelerated simulation marine atmospheric environment, J. Mater. Sci. Technol. 35 (2019) 651–659.
[53] M. Liu, X. Cheng, X. Li, T.J. Lu, Corrosion behavior of low-Cr steel rebars in alkaline solutions with different pH in the presence of chlorides, J. Electroanal. Chem. 803 (2017) 40–50.
[54] E. Sikora, D.D. Macdonald, Defining the passive state, Solid State Ion. (1997) 141–150.
[55] Z. Yang, M. Yu, C. Han, Z. Zhao, X. Jia, M. Zhao, S. Li, J. Liu, Evolution and corrosion resistance of passive film with polarization potential on Ti-5Al-5Mo-^{5}V–^{1}Fe-1Cr alloy in simulated marine environments, Corros. Sci. 221 (2023).
[56] L. Yohai, W. Schreiner, M.B. Valcarce, M. Vázquez, Inhibiting steel corrosion in simulated concrete with low phosphate to chloride ratios, J. Electrochem. Soc. 163 (2016) C729–C737.
[57] W. Zhu, X. Li, C. Zheng, C. Zhang, Q. Mao, Y. Bi, Hydrothermal corrosion behavior of Ti3SiC2 MAX phase at atomic scale under simulated PWR conditions, Corros. Sci. 209 (2022).
[58] Z. Zhang, Y. Qian, J. Xu, J. Zuo, M. Li, Effect of annealing on microstructure evolution and corrosion resistance of an amorphous Cr-Al-C coating, Corros. Sci. 178 (2021).
[59] M. Zhu, R. Wang, C. Chen, H.B. Zhang, G.J. Zhang, Comparison of corrosion behavior of Ti_3SiC_2 and Ti_3AlC_2 in NaCl solutions with Ti, Ceram. Int. 43 (2017) 5708–5714.
[60] L.L. Liu, J. Xu, X. Lu, P. Munroe, Z.H. Xie, Electrochemical corrosion behavior of nanocrystalline beta-Ta coating for biomedical applications, ACS Biomater. Sci. Eng. 2 (2016) 579–594.
[61] D.D. Macdonald, Passivity–the key to our metals-based civilization, Pure Appl. Chem. 71 (1999) 951–978.
[62] P. Marcus, On some fundamental factors in the effect of alloying elements on passivation of alloys, Corros. Sci. 36 (1994) 2155–2158.
[63] W. Li, Z. Wang, J. Shuai, B. Xu, A. Wang, P. Ke, A high oxidation resistance Ti2AlC coating on Zirlo substrates for loss-of-coolant accident conditions, Ceram. Int. 45 (2019) 13912–13922.
[64] Q.-T. Song, J. Xu, TiZrNbTa)90Mo10 high-entropy alloy: electrochemical behavior and passive film characterization under exposure to Ringer's solution, Corros. Sci. 167 (2020).
[65] J. Wang, Y. Zhou, T. Liao, J. Zhang, Z. Lin, A first-principles investigation of the phase stability of Ti2AlC with Al vacancies, Scr. Mater. 58 (2008) 227–230.